# Multi-scale optical coherence tomography imaging and visualization of Vermeer's *Girl with a Pearl Earring*

**TOM CALLEWAERT,**[1,2] **JERRY GUO,**[3] **GUUSJE HARTEVELD,**[2] **ABBIE VANDIVERE,**[4] **ELMAR EISEMANN,**[3] **JORIS DIK,**[2] **AND JEROEN KALKMAN**[1,*] (iD)

[1]*Department of Imaging Physics, Delft University of Technology, Lorentzweg 1, 2628 CJ Delft, The Netherlands*
[2]*Department of Materials Science, Delft University of Technology, Mekelweg 2, 2628 CD Delft, The Netherlands*
[3]*Computer Graphics and Visualization, Delft University of Technology, Van Mourik Broekmanweg 6, 2628 CD Delft, The Netherlands*
[4]*Conservation Department, Mauritshuis, Plein 29, 2511 CS The Hague, The Netherlands*
[*]*j.kalkman@tudelft.nl*

**Abstract:** We demonstrate multi-scale multi-parameter optical coherence tomography (OCT) imaging and visualization of Johannes Vermeer's painting *Girl with a Pearl Earring*. Through automated acquisition, OCT image segmentation, and 3D volume stitching we realize OCT imaging at the scale of an entire painting. This makes it possible to image, with micrometer axial and lateral resolution, an entire painting over more than 5 orders of length scale. From the multi-scale OCT data we quantify multiple parameters in a fully automated way: the surface height, the scattering strength, and the combined glaze and varnish layer thickness. The multi-parameter OCT data of *Girl with a Pearl Earring* shows various features: Vermeer's brushstrokes, surface craquelure, paint losses, and restorations. Through an interactive visualization of the *Girl*, based on the OCT data and the optical properties of historical reconstructions of Vermeer's paint, we can virtually study the effect of the lighting condition, viewing angle, zoom level and presence/absence of glaze layer. The interactive visualization shows various new painting features. It demonstrates that the glaze layer structure and its optical properties were essential to Vermeer to create an extremely strong light to dark contrast between the figure and the background that gives the painting such an iconic aesthetic appeal.

## 1. Introduction

Digital visualization is transforming the study, treatment, and conservation of works of art [1] and opens up new ways to discover their origin, artistic quality, authenticity, and condition. Optical techniques play a key role in capturing the 3D information of works of art that are the basis of digital visualizations [2]. Currently, these techniques have mainly been used to measure the outer surface of an object and not the inside. In addition, the combination of obtaining high resolution data over a large macroscopic work of art is challenging.

Optical coherence tomography (OCT) is a high-resolution imaging application that can image an object's surface and subsurface. OCT has, since 2004, been applied to the analysis of works of art [3–5]. Focusing on the application of OCT to paintings, it has been used for a variety of purposes such as: quantification of varnish drying [6], imaging of underdrawings [7], investigation of canvas deformation [8], control of varnish ablation [9], and examination of stratigraphy [10].

With its high spatial resolution, but limited imaging depth, OCT's main application for painting research is in analyzing thin varnish and glaze layers. Since these layers contribute to the visual appearance of an artwork [11,12] and their condition changes over time, they are of major concern for art conservators and art historians. Common deterioration processes in varnish layers are yellowing, cracking, and loss of transparency, whereas glazes can change color and translucency over time. In general, delamination and paint loss can affect all layers of a painting, but is most evident at its surface. During conservation treatments, conservators may choose to fill and retouch damages in the paint surface and attempt to match the color, topography, and gloss of the surrounding original paint. Varnish layer(s) may be removed and new layers applied to saturate the surface. Prior to the current study, the relatively small scan area of OCT (typically 1 cm$^2$) led to it being used to obtain highly localized information about varnish and glaze layers, i.e., small cross-sectional or volumetric OCT scans are taken at specific locations. Hence, OCT images are generally not used for the purpose of identifying these regions of interest. Instead, the few scan locations are chosen by the naked eye on the original painting, or via images of the painting measured with other techniques such as digital photography, UV-induced fluorescence photography, or (hyperspectral) reflectance imaging. In addition, since only OCT reflectivity scans are made, features that are easily identified from OCT images are typically limited to the stratigraphy. Automatic visualization of features from other properties of the OCT image is currently impossible. Finally, large scale structures extending beyond the typical OCT scan area are not delineated and therefore visualization has been limited to conventional small-scale 2D and 3D images without interactivity.

To address OCT's shortcoming of its small-scan range, attempts have been made to extend it. For example, OCT velocity tracking has been applied to measure high resolution OCT images in handheld mode obtaining cross-sectional scans stretching out over more than 5 cm [13]. In this case the axial (FWHM) resolution was 18 μm and the lateral resolution is 10 μm. Also large volume OCT has been demonstrated that can collect information over a square meter area with large depth range [14]. In this case the axial resolution was limited to 15 μm and a lateral (undersampled) FWHM resolution was 550 μm. More recently, this was improved to an axial resolution of 14 μm and a lateral (undersampled) FWHM resolution of 160 μm over a $0.2 \times 0.2$ m$^2$ area [15]. However, in all of these cases a combination of both high spatial resolution and large-scale imaging has yet remained unfeasible.

In this paper, we present multi-parameter multi-scale OCT (MS-OCT) imaging of the painting *Girl with a Pearl Earring* by Johannes Vermeer (c. 1665, Mauritshuis). Through automated acquisition, image segmentation, and 3D image stitching we acquired a single large OCT volume of 40 cm × 40 cm × 1.89 mm without loss of either axial or lateral resolution, spanning more than 5 orders of length scale. Multi-parameter MS-OCT can visualize large-scale structures such as brushstrokes in underlying layers, identify areas of damage, locate painting restorations, and highlight regions of interest. A physics-based digital rendering of the *Girl* shows how the painting can be virtually studied under different viewing angles, lighting conditions, zoom levels and in the presence/absence of the glaze layer. As such, we can virtually "look over the shoulder of Vermeer" and in a novel way understand Vermeer's painting process and the importance of the glaze layer, which creates an extremely strong light to dark contrast between the figure and the background that gives the painting such a powerful aesthetic appeal.

## 2. *Girl with a Pearl Earring*: conservation and restoration history

Multi-scale OCT imaging and visualization was applied to *Girl with a Pearl Earring* as part of the 2018 technical examination project *The Girl in the Spotlight*, where the painting was examined by an international team of scientists, researchers, and conservators, working within the collaborative framework of the Netherlands Institute for Conservation+Art+Science+ (NICAS) [16].

Prior to this, the painting last underwent a thorough technical examination and conservation/restoration treatment in 1994 [17]. In this study, microscopic samples of the painting were taken, mounted as cross-sections, and analyzed using a variety of scientific methods; these were re-examined in 2018 [16]. This provided information about Vermeer's materials and techniques, especially the stratigraphy and composition of the dark background of the painting [18]. Groen et al. [17] found that Vermeer built up the background on top of the ground layer by applying: a black (charcoal-containing) underlayer, followed by a glaze. A glaze is a (semi-)translucent paint layer that contains pigments or dyestuffs with a refractive index that closely matches the binding medium (in this case, linseed oil). In *Girl with a Pearl Earring*, the glaze contains the colorants indigo (blue) and weld (yellow). The scientists and conservators in 1994 concluded that when Vermeer painted the background, it was an "even, smooth, glossy, translucent, hard green paint, made to look darker and given depth by a dark underpaint" (see [17], p. 178). Over time, the components of the glaze have degraded, so it has become patchy and grayish.

In the three centuries since Vermeer painted *Girl with a Pearl Earring* other changes have occurred due to the natural aging of the painting, the environmental conditions in which it has been kept, mechanical damages, and multiple restoration treatments. Throughout the painting, but especially within her yellow jacket, there are small paint losses where fragments of the original paint (and sometimes ground) layers have become dislodged. During the 1994 restoration treatment (see Fig. 5 in [19] of the pre-1994 treatment state) losses were filled to bring them to the same height as the surrounding original paint. Some older fills from a previous treatment were not completely removed, but instead their height was adjusted. Then they were retouched with a paint made from a synthetic binding medium and dry pigments [17,19,20]. The conservators attempted to match both the topography and the color of the surrounding original paint using so-called "mimetic retouching" [20]. Before and after applying these materials, conservators applied varnish to the surface of the painting to saturate and protect the colors. Regardless of how well a conservator attempts to replicate the color and texture of the surrounding original paint, their retouches will always differ slightly. This is due to the fact that they use modern materials (binding media, pigments and fills) that are more chemically stable than traditional ones, but may differ slightly in their optical and physical properties.

## 3. Materials and methods

The multi-scale OCT scanner setup consists of 3 scanning stages with a motor controller in an *x-y-z* configuration, a spectral-domain OCT setup and a desktop computer that controls the stage movement and the OCT setup. The post processing of data is done on a desktop computer system.

### 3.1. Multi-scale OCT setup

The experiments are performed with a Thorlabs Ganymede-II-HR spectral-domain OCT system operated with home built Labview software. The computer is a Dell precision workstation (T1700) with 16 GB Ram memory, an Intel Xeon E3-1271v3 processor and an added internal 1 TB solid state drive (SSD) (WD Blue 3D NAND) for data storage during measurements. The OCT system has a spectrum centered at 900 nm, spanning a bandwidth of 195 nm. The axial bandwidth-limited resolution is 3.4±0.2 μm (in air), the lateral resolution is 7±3 μm [21]. The spectrometer roll-off is characterized by a ratio of the spectral resolution on the camera over the sampling interval of 0.69 ± 0.05. The signal to noise ratio, determined from an OCT measurement of a single mirror reflector, is 92.4±0.5 dB. The OCT system is operated with a Thorlabs LSM04-BB telecentric imaging lens that has a maximal field of view of 14.1×14.1 mm$^2$. Figure 1(a) shows the OCT system in front of the painting.

To prevent specular reflections from the sample to the detector, which might saturate the camera the OCT probe is slightly tilted. The focal plane of the OCT sample arm optics is set to 0.4 mm below the zero delay position. This is sufficient to avoid sample arm autocorrelation

artifacts in the OCT image, while the remaining imaging range (1.49 mm) is sufficient for imaging the depth profile of paintings. The limited depth range makes it impossible to keep the surface of the object close to focus and the entire sample within the OCT depth range while scanning large areas. We solved this problem by tracking the surface between the acquisition of subsequent C-scans and automatically control the focus position to maintain the top surface of the sample close to zero delay and at the focal plane of the sample arm lens. As a result of the angle between the translation stage and the surface, the surface may shift to larger depths and eventually goes outside the maximum (Nyquist limited) depth range. We detect the position of the surface reflection in the measured A-scan and use that as an indication of the shift value (repositioning of the focal plane) for the next C-scan. If the shift is too small no focal plane repositioning is performed. We repeat this process for every lateral position of the $x-$stage.

For large area scanning the OCT scan probe is mounted on a 3 axis stage consisting of two 20 cm ($x$ and $y$-axis) scan range stages (8MT50-series, Standa) and a 10 cm ($z$-axis) scan range stage (8MT50-series, Standa) mounted in an $x$-$y$-$z$ configuration. The maximum dimension of the scanned surface (limited by the scanning stages) is $20 \times 20$ cm$^2$. The shape of the $x$-$y$ scanning area is rectangular and sampled with C-scans of $5 \times 5$ mm$^2$ scan area. The sampling rate is 8.5 μm in $x$ and 68 μm in $y$, thereby undersampling the object. These sampling rates can be increased to obtain OCT system limited resolution, in the current study they were limited due to the total scan time constraint within the *The Girl in the Spotlight* project. The OCT probe head is mounted to the setup with the aid of a customized mount. This probe mount has 2 degrees of freedom for tilt around the $x$ axis and $y$ axis, enabling imaging of a surface under a small angle, which is necessary to reduce the amount of specular reflection. The OCT probe head and scan system is shown in Fig. 1(b). Control of OCT acquisition and $x$-$y$-$z$ stage control is performed in Labview. Figure 1(c) shows the geometry of a single C-scan with $M = 586$ A-scans in the $x$-direction and $N = 74$ B-scans in the $y$-direction over the $5 \times 5$ mm$^2$ field of view. Figure 1(d) shows a schematic of the scan pattern for a $2.5 \times 2.5$ cm$^2$ scan area. The red dots indicate the center position of the 0.5 cm $\times$ 0.5 cm field of view of the individual C-scans. The red rectangles indicate the individual C-scan size. The index of the C-scan in the $x$-direction by $i$ running to $I$. Similarly, the index of the C-scan in the $y$-direction by $j$ running to $J$.

Large amounts of data are collected during the measurements that need to be stored and processed. Although the OCT data is measured in the C-scan mode of the imaging system, we store the data on a B-scan level. This allows for a queued data stream to the computers' RAM; the data in the RAM from the previous C-scan is written to the SSD, while the new C-scan is already being acquired.
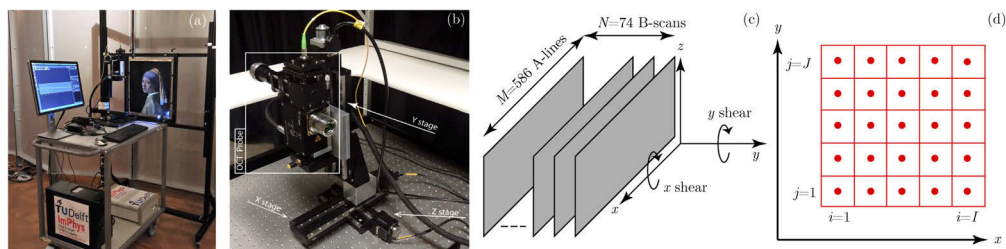


**Fig. 1.** (a) The OCT system during scanning of *Girl with a Pearl Earring*. (b) OCT probe head mounted on $x$-$y$-$z$ scanning stages. (c) Schematic overview of the C-scan OCT scan pattern, the volume is sampled anisotropic. (d) Large-scale OCT scan pattern. The squares indicate individual C-scans centered on the point in the middle of the square.

### 3.2. Multi-scale OCT data processing

A single $20 \times 20$ cm$^2$ OCT scan results in 881.4 GB of single precision float raw data and 215,168 data files (B-Scans). After data acquisition, the data post processing is done with custom written Python software. Since the total size of all the recorded data is too large to be fully stored in the RAM of a regular workstation PC, we use the surface interface in the OCT data as a metric for our image stitching. This reduces the 3D C-scan array to a 2D surface height array. Eventually, after image stitching, the stitched C-scan data is stored in a single PyTable file (Python PyTables package) that can efficiently store the data. The size of the volumetric dataset for a single quadrant is $24026 \times 3034 \times 1024$ voxels (no oversampling) and has a size of 438 GB. Our selected PyTable chunksize is $24026 \times 74 \times 1024$ voxels. This is the equivalent to a 20 cm by 5 mm by 1.9 mm volume of the data of a single quadrant. This chunk contains all successive scans along a full row/column of the unstitched multi-scale C-scan. Whenever possible the data analysis is parallelized over multiple computer cores with the joblib extension package.
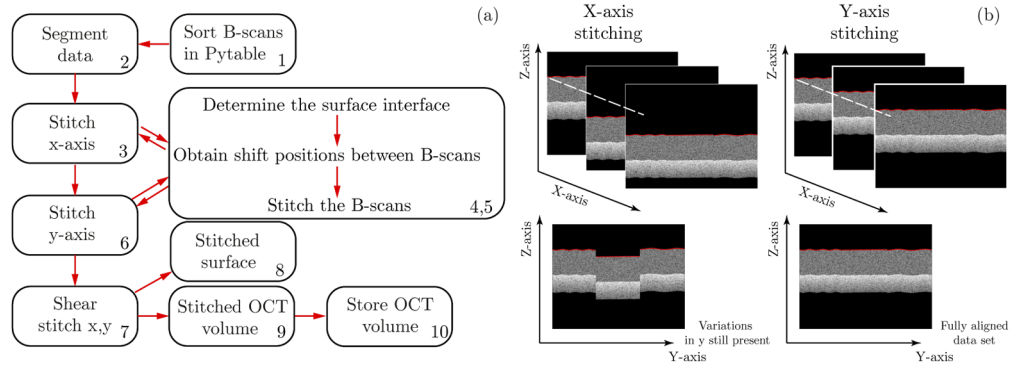


**Fig. 2.** (a) MS-OCT data processing flowchart. (b) Schematic illustration of the *x*-axis and *y*-axis stitching. The surface segmentation is indicated in red.

An overview of the entire OCT post-processing work flow is shown in Fig. 2(a) with the most important steps visualized in Fig. 2(b). Before describing the data processing we first define the following

- the total number of B-scans in the entire object along the *x*-axis is $I$, with a specific B-scan indicated with index $i$, $1 \le i \le I$

- the total number of B-scans in the entire object along the *y*-axis is $J$, with a specific B-scan indicated with $j$, $1 \le j \le J$.

- the number of A-scans in a B-scan is $M$, with a specific A-scan indicated with $m$, $1 \le m \le M$.

- the number of B-scans in a C-scan $N$, with a specific B-scan indicated with $n$, $1 \le n \le N$

The indexation is shown in more detail in Fig. 1(c,d). With these definitions every A-line is uniquely defined by the index pair $((i-1)M + m, (j-1)N + n)$.

After data acquisition and storing sorted unstitched B-scans, we segment the upper interface (surface) of the OCT data (Fig. 2(b)-step 2). The determination of the upper interface is performed for every B-scan by finding the location of highest reflectivity (which occurs at the air-object interface) along the depth axis for every A-scan using our segmentation algorithm [21]. Subsequently, this air-object surface height is stored in a matrix $SC$ at the A-scan location, i.e., $SC((i-1)M + m, (j-1)N + n)$.

Performing a stitching in the *y*-direction is based on first obtaining the *z*-shifts for C-scan block $(i, j)$ by comparing the surface heights at all end points of every B-scan averaged over the *x*-direction and calculating the shift $\Delta S_z(i, j)$ for $j \geq 2$ is determined according to

$$\Delta S_z(i, j) = \Delta S_z(i, j - 1)$$
$$+ \frac{1}{M} \sum_{m=1}^{M} SC((i - 1)M + m, (j - 1)N + 1) - SC((i - 1)M + m, (j - 1)N). \tag{1}$$

In Eq. (1) we have set the starting shift for every $j^{th}$ C-scan in the *x*-direction to zero, i.e., $\Delta S_z(1, 1) = 0$. Subsequently, we stitch the OCT B-scans in the *z*-direction by performing a circular shift operation (Fig. 2(b)-step 3). A similar step is performed in the *y* direction (Fig. 2(b)-step 6). The result is a volume array, in which every C-scan in the multi-scale scan is translated along the *z*-axis to form a complete stitched volume.

We further improve the image stitching by compensating for small angular misalignment between measured C-scans that lead to small (in the order of 1-2 μm) shifts between adjacent C-scans. We attribute these misalignment due to unwanted vibration artifacts during data acquisition. To remove these remaining shifts we add a shear stitching process that shear shifts the individual C-scans along the *x/y*-axis as shown in Fig. 1(c). The shear shift $\Delta S_s(i, j)$ for $j \geq 2$ for the shear in the *y*-direction of every C-scan is

$$\Delta S_s(i, j) = \frac{1}{M} \sum_{m=1}^{M} SC((i - 1)M + m, jN) - SC((i - 1)M + m, jN + 1). \tag{2}$$

Subsequently, the shear is implemented on every A-line of the C-scan using linear interpolation, which, for the *y*-direction, is

$$\Delta S_z((i - 1)M + m, (j - 1)N + n) = \Delta S_s(i, j) \frac{m}{M}. \tag{3}$$

A similar step is subsequently performed in the *x* direction. The result is a volume array where every C-scan in the multi-scale scan is tilted along the *x* and *y*-axis to form a complete stitched volume. Note that the amount of shear stitching shift is only in the order of a few micrometer, which, however, it is essential to completely remove the grid-like pattern as shown in Fig. 3(a).

After termination of the stitching algorithm we obtain the stitched surface and use these positions to shift all the measured B-scans into their proper place (Step 8). Additionally, we can use the result of Step 7 to stitch the C-scan volume data (Step 9) and store the stitched multi-scale C-scan in a PyTable (Step 10). All OCT scans larger than the individual C-scan size with area $5 \times 5$ mm$^2$ in Fig. 3–6 and are stitched with this algorithm.

For a stitched OCT scan of a flat object the reconstructed surface should be flat and not show the individual C-scans. We tested the performance of the image stitching algorithm for a planar sample with a 10×10 cm$^2$ grounded unpainted canvas fixed to a thick cardboard plate. The height of the raw data in Fig. 3(a) clearly shows a mosaic of squares that are associated with the individual C-scans. After application of the stitching algorithm the height of the surface does not show these artifacts any more demonstrating the good quality of our image stitching, as shown in Fig. 3(b). Moreover, in this image modulations of the order of 55 μm are visible that are caused by threads of the canvas visible through the thinly-applied ground layer.

### 3.3. Multi-parameter OCT imaging

From the multi-scale OCT data three parameters are calculated: sub-surface scattering strength, surface height, and glaze+varnish layer thickness.
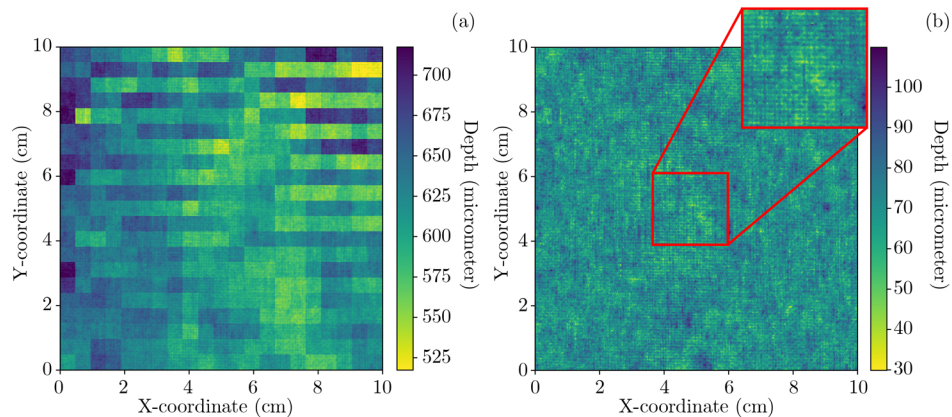
**Fig. 3.** Surface topology of a modern grounded canvas imaged with our multi-scale OCT approach. (a) Surface height before stitching. (b) Surface height after stitching. In an enlargement of the center part of the canvas, the regular pattern of the woven threads are clearly visible.

Surface height, denoted as $z_{\text{air/varnish}}$, is the optical path length of the first segmented air/varnish interface to the OCT zero delay point. Since the surface is in air, this is equivalent to the physical distance of the surface to the zero delay point. The OCT scattering strength $i_{\text{scat}}$ is determined by summing the OCT signal of the first 50 pixels in depth (approximately 100 μm) starting at the pixel position of the air/varnish interface, $i_{\text{scat}} = \sum_{i=0}^{i=50} |i_{\text{OCT}}(z_i)|^2$, with $i_{\text{OCT}}(z_i)$ the complex-valued OCT signal at $z_i$ with the start of the summation at $z_0 = z_{\text{air/varnish}}$. This is similar to the depth averaging [7] or summed voxel projection [22], but in this case is aimed at creating scattering contrast in the near surface region.

The optical thickness of the glaze+varnish layer is determined by segmenting the glaze/black underlayer interface using the segmentation of the first layer as input. Plotted thicknesses stated in this work are OCT optical path length differences, the physical thickness $d$ of the glaze+varnish layer is calculated from the difference between the optical path length depths of the two interfaces with $d = (z_{\text{glaze/underlayer}} - z_{\text{air/varnish}})/n$, with $n$ the refractive index of the medium. All OCT data sets are registered to a reference visible light photographic image of the painting using a custom written Python algorithm that is based on template matching between the photograph and the OCT scattering strength image using scaling and translation of the OCT data.

### 3.4. Digital visualization of the Girl

A digital visualization of *Girl with a Pearl Earring* is made based on the stratigraphy determined with OCT. This is combined with the optical properties of reconstructions of the glaze using historically appropriate pigments.

#### 3.4.1. Stratigraphy reconstruction

On top of the ground layer, the dark background of the *Girl* is built up from: a black underlayer and a glaze layer (applied by Vermeer), with thin varnish layers on top (applied during the 1994 restoration). The main components of the glaze are weld (yellow) and indigo (blue) [17], mixed in roughly 20:1 ratio. Also other components such as red ochre and a drying agent (copper) are present in the glaze, but these are assumed to not affect the optical properties [17,18]. The layered structure of the dark background of the *Girl* is reconstructed using historically appropriate materials [23] with ingredients similar to the ones used by Vermeer with the following recipes

- Underlayer: 0.502 g charcoal black from beech (47800, Kremer Pigmente GmbH & Co.) mixed with 0.570 g linseed oil

- Weld: 0.203 g Weld + potash and $CaCO_3$ (made following a 17th-century recipe), mixed with 0.100 g linseed oil.

- Indigo: 0.500 g indigofera tinctoria (Couleur Garance), mixed with 0.515 g linseed oil.

### 3.4.2. Paint optical properties

The optical properties of the layers in the reconstruction are determined using bidirectional reflectance distribution function (BRDF) measurements of the reconstruction canvas. The measurements are done at the Spanish Council for Scientific Research's Optics Institute (IO-CSIC) in Madrid. The BRDF is measured as a function of wavelength and angular distribution under illumination angles of 15°, 45° and 75°. At every illumination angle the observation angle is varied from 0° to 75° at 5° intervals. For the dark pigment of the dark underlayer the surface appears largely smooth and diffuse; the glaze layer has a much more specular reflectivity.

### 3.4.3. 3D digital visualization

The digital visualization is based on three sets of data: height of the painting surface, the thickness of the glaze layer obtained from the segmented MS-OCT data, and a co-registered RGB image. The height of the painting without the glaze layer is then derived by subtracting the thickness of the glaze from the painting surface. The painting is then a stacked result of the canvas at the bottom, a pigment layer in the middle and a glaze layer on top. The height information of each layer is further processed and two triangulated meshes of the interfaces are generated.

The measured BRDF data is fitted to the analytic GGX [24] microfacet reflection model [25–27]. The microfacet reflection model treats surfaces as a composition of many small flat faces that are invisible from a macro level, and models the surface roughness through a distribution of reflected directions with regard to incoming light and the geometry normal. For our BRDF models, the fit resulted in a roughness parameter of $\alpha = 0.05$ for the glaze layer and a roughness parameter $\alpha = 0.5$ for the pigment layer. The glaze layer thickness is calculated from the optical path length of the layers by using a refractive index of $n = 1.5$ [28]

The painting is rendered in realtime using the OpenGL programming language to achieve an interactive visualization of the dataset. The resolution of the scanned region (few gigabytes) is computationally heavy and based on the fact that detailed features, such as brushstrokes on the painting, never cast shadows onto the painting itself, we use a plane mesh together with a high resolution ($4096 \times 4096$) normal map and a map to mimic small-scale roughness variations (<0.15) . Hereby, we can show the details of the scan without putting too much computational pressure on the hardware. Normal maps add the visual effect of geometrical details without changing the topology of the mesh [29]. When shading a certain fragment (pixel), instead of using the normal information encoded in the geometry, the normal is retrieved from a separate image, the normal map. Using the so-reconstructed normal, reproduces the appearance of the original geometry when it interacts with the light incident on the painting.

## 4. Results

### 4.1. Large-scale OCT imaging

Figure 4 shows the three parameters represented at the largest scale of our MS-OCT technique. The surface height image of the MS-OCT data, Fig. 4(a), shows the variation in the surface height over the painting. Blue areas represent parts that are deeper. On a large scale the height of the background is quite flat without major bulges. The area of the collar can be observed at 'A' where the surface is higher and its height is more varying than that of its surrounding. In this

area Vermeer painted more thickly (impasto), which can be observed from the smaller depth. Over almost the entire painting, a network of cracks (the craquelure) is visible in the image. In addition, we observe many localized paint layer losses scattered over the painting: a few of the most prominent are indicated with circles.
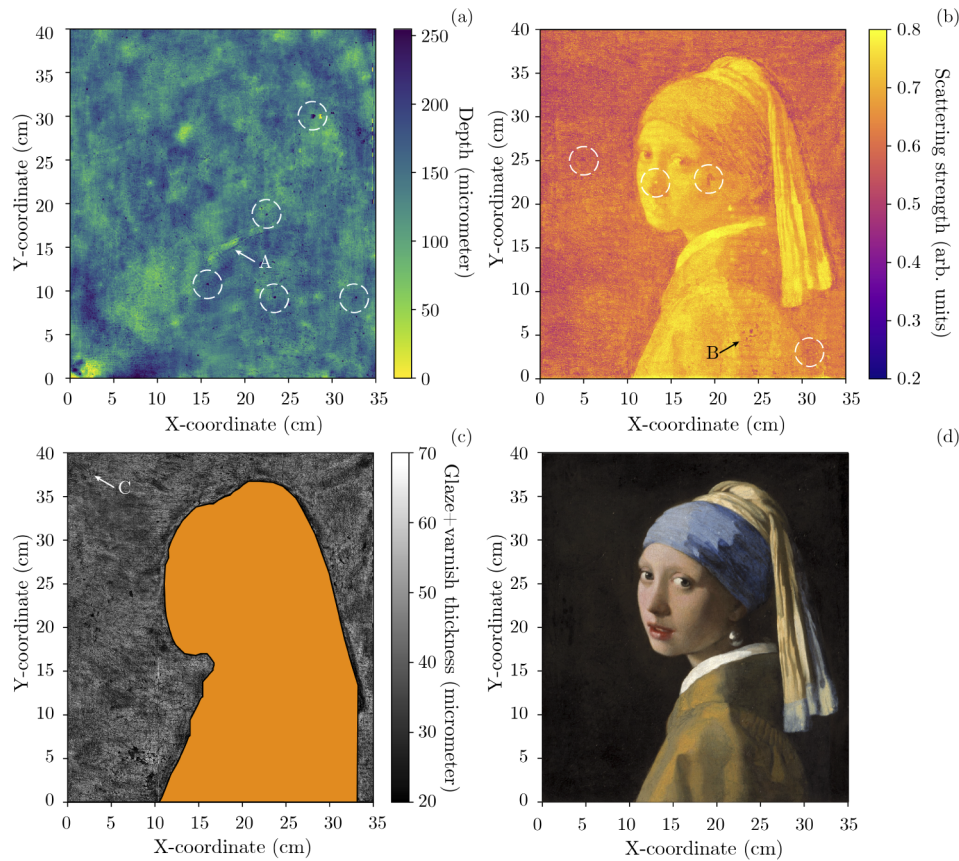


**Fig. 4.** Large-scale OCT imaging results on the scale of the entire painting. (a) Surface height of the painting with paint losses indicated by circles and 'A' indicating an elevation in the surface. (b) Scattering strength image with a few restorations indicated by circles and 'B' indicating a restoration area. (c) Glaze+varnish layer thickness in the background section of the painting with 'C' indicating Vermeer's brushstrokes. The region where no glaze+varnish layer thickness can be determined is indicated in orange. (d) Visible light photograph of *Girl with a Pearl Earring* (Mauritshuis).

The scattering strength image of the multi-scale OCT data, Fig. 4(b), bears a resemblance to the visible light photograph. In general, bright structures observed in the photograph can be traced to areas with strong scattering strength. A restoration can be observed in 'B' where the scattering is not well reproduced. Moreover, in the scattering strength image many more points of restoration are visible at locations where the painting had damages before being restored in 1994.

The glaze+varnish layer thickness image, Fig. 4(c), shows that the glaze layer is present over the entire black background of the painting. There are glazes in other areas of the painting than the background, e.g., in her headscarf and lips, but at these locations the second interface is less visible, causing our algorithm to fail in accurately determining the thickness. The average glaze+varnish thickness, determined over 2427200 A-lines, is 37 ± 9 μm optical path length. Since this includes a varnish layer of approximately 10 μm optical path length, conversion of the

remaining optical path length to physical thickness with a refractive index $n = 1.5$ [28] leads to an average glaze physical thickness of around $20 \pm 6$ μm. This is in reasonable agreement with the value found earlier from a cross-section [16]. Moreover, at multiple locations, the glaze+varnish layer thickness reveals the brushstrokes of Vermeer as these are delineated by areas of striped thickness profiles that are most clearly seen at 'C'. These structures are much less apparent in the surface topography. In summary, our approach makes many structures and features visible that cannot, or are difficult to observe in the conventional visible light photograph.

Although these images give a good impression of the overall state of the painting and indicate specific regions of interest, they do not have the required detail to provide more specific information. Therefore, it is essential to also look at the data in medium-scale OCT, which allows us to examine specific areas, that have been selected from the large-scale images, more closely.

### 4.2. Medium-scale OCT imaging

From the regions of interest observed in the large-scale images we first focus on the ability of our OCT system to image Vermeer's brushstrokes. The glaze+varnish layer thickness image in Fig. 5(a) shows brushstrokes that are barely visible in the air/varnish interface. They also can be well observed in the glaze/black underlayer pigment interface image, but not in the surface height image. This indicates that the glaze flattens the surface. This is shown in more detail in Fig. 5(b) where the painter's brushstrokes are clearly defined throughout the entire glaze+varnish thickness map, best visible at location 'A'. Note that the image in Fig. 5(a) encompasses the location of Vermeer's signature. In the OCT height, thickness or scattering images, Vermeer's signature is not visible.

Figure 5(c) shows the surface height and scattering strength of a part of the collar of the *Girl*. We find that the surface of the painting contains a large number of cracks, edges, and ridges. In response to changing environmental conditions or external forces, cracks can form in paint layers due to expansion and contraction of layer(s) beneath the paint surface. The OCT height image shows that each "flake" of paint is higher at the edges, and lower in the middle: so-called "cupping". The collar of the *Girl* may have been affected by external forces that caused the paint to crack differently than the surrounding paint, and for some paint to even have become dislodged. At location 'B' the original paint has been lost; it was filled during a restoration treatment (before 1994), then during the 1994 treatment the fill was brought to the correct level and retouched. Although the area is visually indistinguishable from the surrounding original paint in normal light, its slightly different topography and scattering can be detected with OCT. In the OCT height image this location is identified by a larger depth indicating a lower surface. In the scattering strength image, the collar at this location has a larger scattering strength than its surrounding indicating that a more reflective pigment (probably titanium white) was used to match the lead white paint that Vermeer used in the collar.

Figure 5(d) shows an OCT scattering strength image of the lower part of the painting. In this image the contrast of the scattering strength image was rescaled (compared to Fig. 4(b)) to include all intensities that fall within the 2nd and 98th intensity percentiles. In this way it more clearly shows the anomalous regions in the painting and, more importantly, it demonstrates the versatility of our method to digitally optimize the identification of important regions of interest. We find several areas where the scattering strength is different to its surroundings. These spots are areas where the painting was damaged and later retouched, again something that is difficult to assess from only the visible light photograph. Although the matching of height and scattering was near perfect we were still able to detect these restorations with MS-OCT.

For further detailed investigation we can select regions with particular small details that are (almost) at the level of an individual OCT C-scan. However, these points and their exact location are only discovered when the painting was imaged and analyzed at its large or medium scale with the multiple parameters we determined from the OCT data.
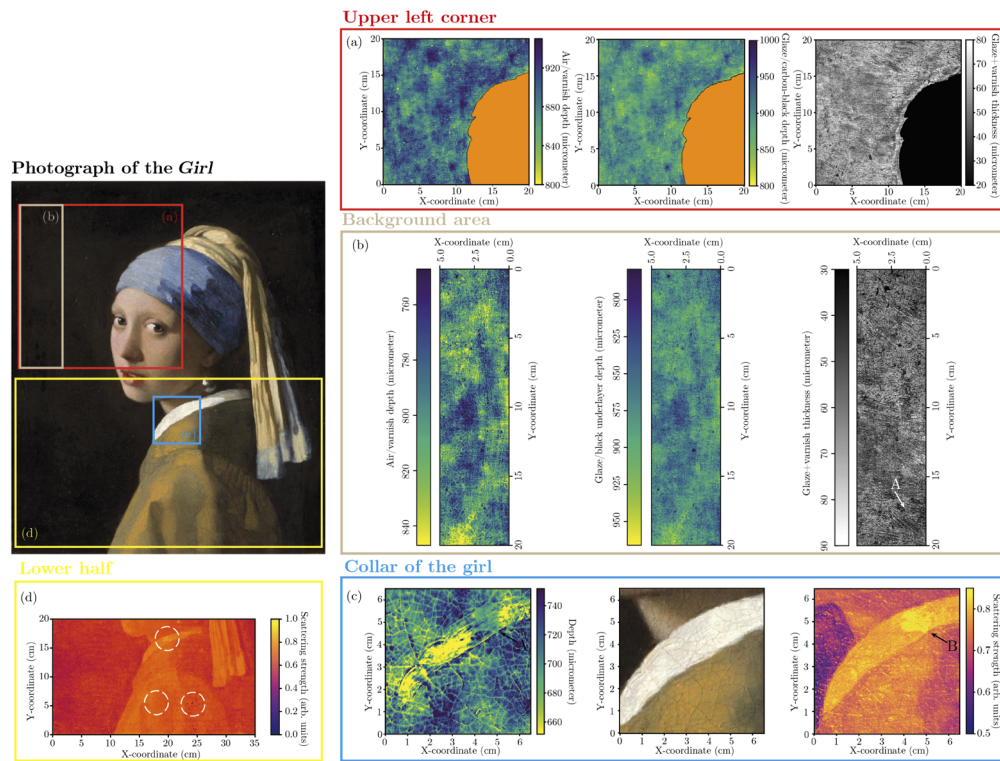
**Fig. 5.** Overview of medium-scale OCT images of regions of interest on the painting indicated by the color of the boxes and letters on the visible light photograph. (a) Surface topology of the first painting interface (air/varnish interface), second interface (glaze/black underlayer pigment), and glaze+varnish layer thickness for an area in the upper left corner. (b) Similar as (a) but for a smaller section clearly showing Vermeer's brushstrokes, indicated by 'A'. (c) OCT images of the collar showing features such as cracks and restorations that are not visible in the visible light photograph, 'B' indicates a restoration area. (d) Contrast optimized scattering strength image of the bottom half of the painting showing areas where original paint material has been lost and restorations have taken place (indicated with circles).

## 4.3. Small-scale OCT imaging

To give an indication of the OCT images obtained from the painting *Girl with a Pearl Earring* we show individual B-scans and small-scale stitched OCT images.

Figure 6(a) shows an area in the background of the painting. In this case the top surface and the scattering strength image do not indicate any notable features. However, the glaze/black underlayer interface shows a feature, which is even more clearly visible in the glaze+varnish thickness map. From these images we conclude that a fragment of paint has come off in the past. Subsequently, the loss was filled with a highly scattering material, retouched with a semi-translucent paint, and a varnish layer was applied on top [19]. Although the matching of height and scattering strength was near perfect to the naked eye we are still able to detect this from the depth profiling ability of OCT.

Also at this scale, we can study traces of damages and former restoration materials in greater detail. Figure 6(b) shows an area in the coat of the *Girl* that was filled in a treatment before 1994, then retouched in 1994. In the visible light photograph, the restoration is almost invisible, suggesting that the topography and color of the retouching was matched very accurately to the surrounding paint. With OCT, the height profile shows that the surface height of the fill has
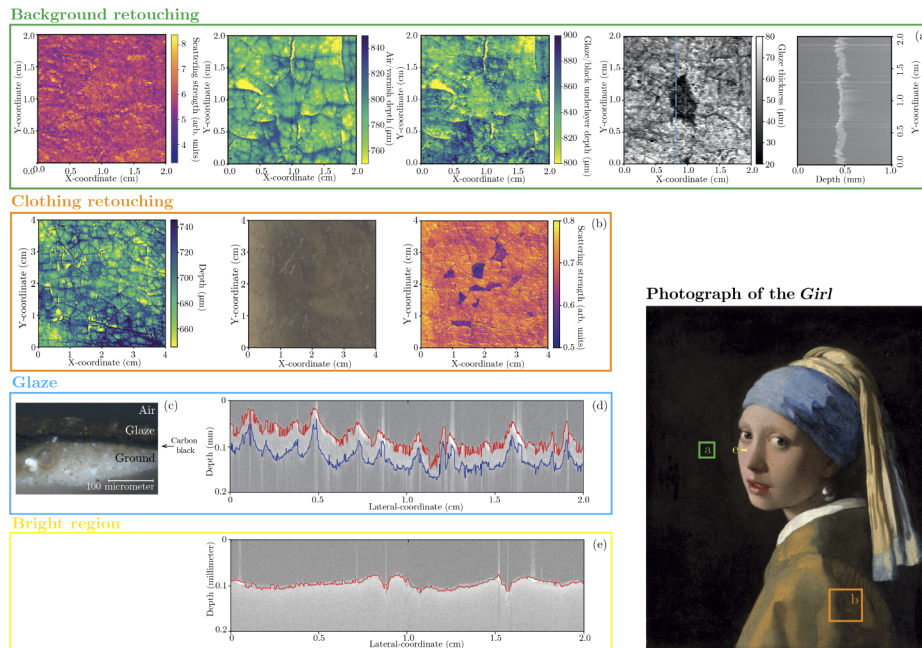
**Fig. 6.** Overview of small-scale OCT images of regions of interest in on the painting indicated by the color of the boxes and letters in the visible light photograph. (a) Small-scale OCT data demonstrating paint loss in the background. The glaze+varnish layer thickness image clearly shows a much thinner layer present at the surface. The OCT cross-sectional image, taken at the location of the dashed line, shows that the original layers are absent and replaced by a strongly scattering fill. (b) Small-scale OCT data of an area of loss in the clothing of the *Girl*, which was restored in 1994 (visible light image contrast enhanced). Scattering strength image clearly shows the location of restorations whereas this is not visible in the height and visible light photograph. (c) Paint cross-section analyzed with brightfield microscopy [18], figure courtesy Annelies van Loon (Mauritshuis/Rijksmuseum). (d) OCT cross-section close to the location where (c) was taken, with air/varnish (red) and glaze/black underlayer (blue) interface segmentation indicated. (e) OCT cross-section in the face of the *Girl*, with segmented air/varnish interface (red) indicated. Note the absence of multiple interfaces in the face of the *Girl* due to the presence of a strongly scattering surface layer.

accurately matched that of the surrounding original paint, hence, the restoration is not noticeable in the visible light photograph. However, the scattering strength OCT image shows that the restoration has not exactly reproduced the scattering of the original painting. This is because the synthetic binding medium and the slightly different pigment mixture used in the retouching scatters light differently than the surrounding original paint.

For reference, we also show OCT cross-sections of the glaze and bright region. Figure 6(c) shows a paint cross-section analyzed with brightfield microscopy (sample number 19 indicated in Fig. 13 in [17]). Figure 6(d) shows the OCT cross-section taken in close vicinity. In both the brightfield microscopy and the OCT image, the glaze layer can be well delineated. In the OCT image the layer below the black underlayer is dark, indicating very little light transmission into this region. The high intensity peaks are due to strong specular reflections that despite the angular offset partly saturates the detector. Figure 6(e) shows an OCT cross-section from the face of the *Girl*. A thin varnish layer is visible on top of a continuous scattering layer. The OCT signal at large depths is mainly multiple scattered light.

In summary, MS-OCT can image over multiple length scales with multiple contrast mechanisms over an entire macroscopic painting. A movie of the multi-scale multi-parameter OCT data set of the *Girl* is available as Visualization 1.
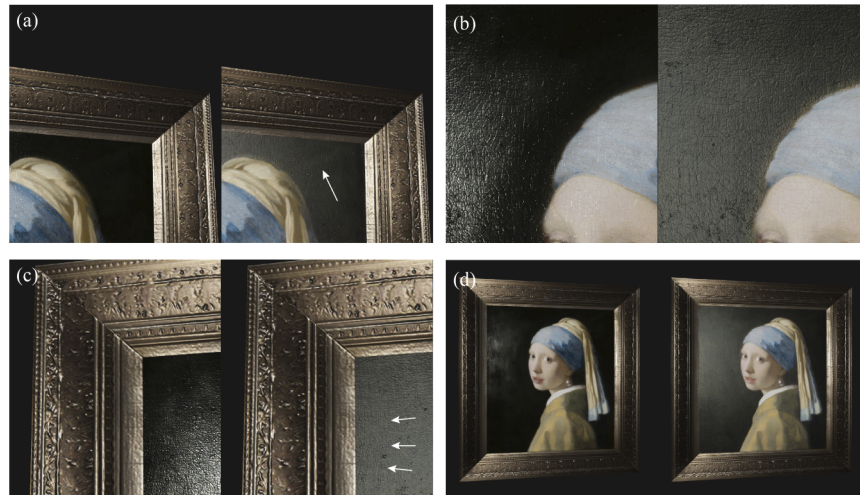
### 4.4. Virtual rendering of the Girl



**Fig. 7.** Screenshots of our interactive visualization of the *Girl*. (a) In the visualization with no glaze present, slight variations in color are faintly visible as diagonal lines (indicated with arrow). (b) Strong visibility of crack patterns in the visualization with no glaze present. (c) Pronounced thread cusping visible in the no glaze state (indicated with arrow). (d) Oblique view on the painting demonstrating the lower contrast when the glaze layer is absent.

The MS-OCT data also allows for a virtual assessment of the painting's appearance both with and without the the glaze layer in the background. We made a digital reconstruction of the painting based on the MS-OCT data sets of the air/varnish height and the glaze/black underlayer height. This information is complemented by the bidirectional reflection distribution function (BRDF) of paint reconstructions [18]. Together these data are used to render a physics-based and historically approximate representation of the painting under ambient lighting conditions. Moreover, it is possible to interactively vary the lighting conditions, viewing angle, zoom level, and the effect of the presence/absence of the glaze layer. Hereby, we can virtually "look over the shoulder of Vermeer" and view the painting in different conditions before its final state. Figure 7 shows screenshots of our digital representation, where the painting of the *Girl* with the glaze (left) and no glaze (right) are rendered interactively side by side. In (a) we visualize that the glaze somewhat obscures light and dark differences in the background, which have been interpreted to be the folds of a curtain [16]. It also changes the mat into a specular appearance (b), obscures the visibility of thread cusping (c), and enhances the overall contrast between figure and background (d). An impression of the interactive demo is available as Visualization 2.

## 5. Discussion

For the first time, we are able to perform high resolution depth resolved imaging and visualization at the scale of an entire macroscopic painting. With our technique we make it possible to observe the object both at the macroscopic and the microscopic scale, with different types of contrast, under varying lighting conditions, and with varying layer composition.

## 5.1.   Application of MS-OCT on the Girl

We demonstrate that with multi-parameter MS-OCT imaging that it is possible to clearly identify important regions of interest such as retouchings and losses in the painting in places where one would not expect them based on the visible light photograph alone. MS-OCT can detect these locations because the binding medium and some pigments used by conservators differ from the materials originally used by the original artist. For example, in the OCT scattering strength image many of the fills and retouchings applied during the 1994 restoration treatment [19] can be identified. With MS-OCT we can pinpoint these locations in the OCT images and zoom in for more detailed analysis. Our approach is especially suited to identify restorations based on scattering strength, surface height, glaze thickness, or a combination of these. Given the relative low sampling density we estimate that with a higher sampling density almost all of the retouchings and fills can be identified with the scattering strength contrast. Hence, potentially OCT even can complement or replace existing techniques to verify the claimed origins of cultural heritage by making visible previous (concealed) restorative efforts to the assessors at locations where unusual scattering properties are expressed.

The interactive visualization clearly shows how different features such as brushstrokes, the thread cusping of the canvas, and variations in color of the background are masked by the background's green glaze layer. The merit of our virtual reconstructions is that they allow for a clear visualization of these optical effect. Our visualization shows that under appropriate lighting conditions, the background becomes a deep dark without the characteristics of a rough painted surface. OCT visualization of the glaze + varnish thickness detected pronounced brushstrokes in the background at the edges of the painting where, we assume, Vermeer used narrower brushes to keep the paint within the perimeter of the composition. Since the brushstrokes in these areas are more clearly defined in the glaze+varnish layer thickness it is evident that this layer combination reduces the surface roughness of the paint layer. As was also concluded by Vandivere et al. [18], the glaze layer therefore has two functions. First, it limits the amount of light observed originating from the black underlayer. Second, the glaze layer smooths out the surface thereby reduces the visibility of any brushwork as the reflection becomes more specular. Hence, the combination of underlayer and glaze maximizes the darkness of the *Girl's* background, which is well visible in our virtual reconstruction.

This background stands in sharp contrast with the *Girl's* brightly lit figure and demonstrates how essential the glaze layer is in reaching this effect. The bright parts are composed of the most reflective paint, as seen in Fig. 4(b). In the lightest part of the painting, the *Girl's* collar, Vermeer deliberately used pronounced impasto in his painting. The paint topography map of Fig. 4(a) shows contour lines of the *Girl's* collar. While the absence of surface topography in the background increases the illusion of deep darkness, the opposite applies to the collar. Here, a deliberately pronounced and structured surface topography creates the pictorial suggestion of a white textile with light reflections. These examples show how Vermeer was in full control of the optical characteristics of his paint —on, at and below the paint surface. The OCT data show how the artist exploits paint translucency, reflectiveness and topography in his effort to maximize the pictorial illusion of reality. Vermeer used all these optical effects to create the dramatic lighting of the painting with a strong contrast between the dark background and the figure. This contrast has been crucial in creating the impression of a girl who suddenly and spontaneously turns towards the viewer from deep darkness. Vandivere et al. [18] speculated that this strong contrast and limited dynamic range in the painting may have been inspired by advances in lens technology, perhaps the use of a camera obscura, which has been associated earlier with Vermeer's work [30].

The surface height measurements of *Girl with a Pearl Earring* make it possible to examine the paintings craquelure at high detail. This is of great importance to document the physical state of the painting. OCT can provide height maps with an accuracy of the order of the axial resolution

(2-3 µm) and performs, in this respect, better than several other techniques [31]. In particular OCT provides both excellent surface height accuracy and high resolution depth sectioning. In the *Girl*, the craquelure exhibits different characteristics throughout the painting, which suggest various mechanism for their formation [32]. Moreover, the height information together with the OCT thickness information enables the detailed analysis of the crack formation process [33].

## 5.2. MS-OCT technology

For the current painting, the height and thickness determination is based on our segmentation algorithm, which works well since the build-up of the painted object in the background is well defined —black underlayer, glaze layer, thin transparent varnish layers —as shown Fig. 6(c-d). The glaze/black underlayer interface is very distinct due to complete absorption of light by charcoal at the interface position. For the area with the figurehead the second interface was difficult to detect and a glaze layer thickness determination was impossible.

The MS-OCT system operates at system-limited spatial resolution, albeit that the image is undersampled in both lateral directions to reduce the total scan and data transfer time. However, there is no fundamental limitation in the image sampling, and the sampling rate was only constrained by the total imaging time available. Also in other large scale OCT approaches [14,15] significant undersampling is present. An important distinction to this work is that this work focuses on high axial resolution imaging of thin layers based on a spectral-domain OCT system. Since spectral-domain OCT detection is incompatible with the large depth range swept-source detection, the object has to maintained close to zero delay and hence both the axial and lateral resolutions are much higher than in large distance OCT scanning, albeit at the cost of longer acquisition times. When applying more dense sampling we expect many more small scale features to be better visible.

Although the net OCT imaging time for the entire painting is 24 hours, the most time consuming step is the transfer of data to computer RAM and SSD between successive C-scans (approximately 66% of total data acquisition time). Consequently, the use of faster storage drives would significantly speed up the acquisition time. Furthermore, since for the application to painting imaging only a small depth section is of importance, a Fourier transform and depth selection (aided by information provided by the focus control algorithm) performed directly after acquisition could significantly reduce the data throughput, we estimate for our set-up at least by a factor of ten. The current post acquisition data analysis time is 48 hours for the entire painting. Further increasing the number of CPU or GPU cores can reduce analysis times as the data processing is well suited for parallel computation.

## 5.3. MS-OCT application

The demonstrated 3D stitching algorithm, for axial translation and small angular rotation, may be applied to other depth-resolved methods such as confocal microscopy and multi-photon microscopy. Also for these techniques, a clearly delineated interface that is segmented, can be used for the stitching process and contribute to increase the imaged volume.

Our registration method is of great importance to co-locate the data to the correct position. We found that also images of modalities such as X-ray fluorescence (XRF) and infrared imaging can be registered with our algorithm to the visible light photography image as their overall contrast has a shape similarity to the visible light photograph (bright/dark corresponds to bright/dark, or dark to bright and vice versa). The registration algorithm is found to be very robust and always converged to, what to the human observer is, the correct image overlap. Employing image stitching and registration, we envision multi-parameter OCT data and multi-modal data (e.g. XRF) to be placed in a single software environment for virtual manipulation, study, and visualization. Since every imaging modality technology gathers complementary information of

the artwork, the virtual representation of multi-channel information will lead to novel insights in artwork condition and composition.

MS-OCT can be of great importance for art historians, art dealers, and painting conservators. For art historians stratigraphy data and its digital visualization may provide more information about the artistic qualities that are being used to create specific painterly effects with thin varnish and glaze layers. For example, early Netherlandish paintings, which often exploit the properties of translucent glazes over opaque underlayers, might be good candidates for this approach [34]. For art dealers, it would be of great benefit to use multi-parameter OCT to identify restorations even if they are hidden under the surface or concealed by thin layers.

We view the greatest potential for our work in the hands of art conservators. While imaging smaller sections, our technique can provide real-time information about the varnish and glaze layer stratigraphy during conservation treatment, especially during varnish removal. More importantly, whole-painting OCT acquisition, image segmentation, and image analysis can be of paramount importance to improve our understanding of artworks and the effects of conservation/restoration efforts. In the past decades, various forms of point analysis used in the examination of artworks, and notably paintings, have been transformed into full-scale imaging methods. This applies, e.g., to MA-XRF [35] and MA-XRPD [36] scanning, which were first applied in cultural heritage studies at synchrotron facilities, but have been transformed into user-friendly and mobile counterparts that are now routinely used in museum conservation studios for the scanning of many square meters of historical paintings. Similar developments can be seen in the field of NIR and hyperspectral imaging. These developments show the clear and structural demand in heritage science for art conservationists to document and monitor -integrally and at high resolution- the material condition of artworks. We foresee a similar development for MS-OCT in the cultural heritage field. With its capability to chart the paint surface and its superficial stratigraphy, including glaze layers and varnish layers, it is complementary to the non-destructive imaging methods mentioned above will become a valuable tool for the integral, full-scale analysis of historical paintings and other museum objects.

## Funding

## Acknowledgements

## Disclosures

The authors declare no conflicts of interest.

## References

1. F. Windhager, P. Federico, G. Schreder, K. Glinka, M. Dörk, S. Miksch, and E. Mayr, "Visualization of cultural heritage collection data: State of the art and future challenges," IEEE Trans. Visual. Comput. Graphics **25**(6), 2311–2330 (2019).

2. G. Sansoni, M. Trebeschi, and F. Docchio, "State-of-the-art and applications of 3D imaging sensors in industry, cultural heritage, medicine, and criminal investigation," Sensors **9**(1), 568–601 (2009).

3. P. Targowski, B. Rouba, M. Wojtkowski, and A. Kowalczyk, "The application of optical coherence tomography to non-destructive examination of museum objects," Stud. Conserv. **49**(2), 107–114 (2004).

4. M. L. Yang, C.-W. Lu, I.-J. Hsu, and C. C. Yang, "The use of optical coherence tomography for monitoring the subsurface morphologies of archaic jades," Archaeometry **46**(2), 171–182 (2004).

5. H. Liang, R. Cucu, G. M. Dobre, D. A. Jackson, J. Pedro, C. Pannell, D. Saunders, and A. G. Podoleanu, "Application of OCT to examination of easel paintings," Proc. SPIE **5502**, 378 (2004).

6. H. Liang, R. Cucu, G. M. Dobre, D. A. Jackson, J. Pedro, C. Pannell, D. Saunders, and A. G. Podoleanu, "Optical coherence tomography: a non-invasive technique applied to conservation of paintings," Proc. SPIE **5857**, 58570W (2005).

7. A. Podoleanu, H. Liang, M. G. Cid, R. Cucu, G. Dobre, J. Pedro, and D. R. Saunders, "In-fiber optical coherence tomography for examination of paintings," Proc. SPIE **6004**, 600401 (2005).

8. P. Targowski, M. Góra, T. Bajraszewski, M. Szkulmowski, B. Rouba, T. Łękawa-Wysłouch, and L. Tymińska-Widmer, "Optical coherence tomography for tracking canvas deformation," Laser Chem. **2006**, 1–8 (2006).

9. M. Góra, P. Targowski, A. Rycyk, and J. Marczak, "Varnish ablation control by optical coherence tomography," Laser Chem. **2006**, 1–7 (2006).

10. P. Targowski, M. Iwanicka, L. Tymińska-Widmer, M. Sylwestrzak, and E. A. Kwiatkowska, "Structural examination of easel paintings with optical coherence tomography," Acc. Chem. Res. **43**(6), 826–836 (2010).

11. E. R. de la Rie, "The influence of varnishes on the appearance of paintings," Stud. Conserv. **32**(1), 1 (1987).

12. J. K. Delaney, E. R. de la Rie, M. Elias, L.-P. Sung, and K. M. Morales, "The role of varnishes in modifying light reflection from rough surfaces - a study of changes in light scattering caused by variations in varnish topography and development of a drying model," Stud. Conserv. **53**(3), 170–186 (2008).

13. N. Weiss, T. G. van Leeuwen, and J. Kalkman, "Doppler-based lateral motion tracking for optical coherence tomography," Opt. Lett. **37**(12), 2220 (2012).

14. Z. Wang, B. Potsaid, L. Chen, C. Doerr, H.-C. Lee, T. Nielson, V. Jayaraman, A. E. Cable, E. Swanson, and J. G. Fujimoto, "Cubic meter volume optical coherence tomography," Optica **3**(12), 1496 (2016).

15. S. Song, J. Xu, and R. K. Wang, "Long-range and wide field of view optical coherence tomography for in vivo 3D imaging of large volume object based on akinetic programmable swept source," Biomed. Opt. Express **7**(11), 4734 (2016).

16. A. Vandivere, J. Wadum, K. J. van den Berg, and A. van Loon, "From 'Vermeer illuminated' to 'The Girl in the Spotlight': approaches and methodologies for the scientific (re-)examination of Vermeer's Girl with a Pearl Earring," Heritage Sci. **7**(1), 66 (2019).

17. K. M. Groen, I. D. van der Werf, K. J. van den Berg, and J. Boon, "Scientific examination of Vermeer's "Girl with a Pearl Earring' (Dutch portraiture)," Studies in the History of Art **55**, 169–184 (1998).

18. A. Vandivere, A. van Loon, T. Callewaert, R. Haswell, A. N. P. Gaibor, H. van Keulen, E. Leonhardt, and J. Dik, "Fading into the background: the dark space surrounding Vermeer's Girl with a Pearl Earring," Heritage Sci. **7**(1), 69 (2019).

19. J. Wadum and N. Costaras, "Johannes Vermeer's "Girl with a Pearl Earring" de- & re-restored," Restauration, Dé-restauration, Re-restauration, Preprints of ARAAFU (1995).

20. J. H. Stoner and R. Rushfield, *Conservation of easel paintings: principles and practice* (Butterworth-Heinemann, 2012).

21. T. Callewaert, J. Dik, and J. Kalkman, "Segmentation of thin corrugated layers in high-resolution oct images," Opt. Express **25**(26), 32816 (2017).

22. D. C. Adler, J. Stenger, I. Gorczynska, H. Lie, T. Hensick, R. Spronk, S. Wolohojian, N. Khandekar, J. Y. Jiang, S. Barry, A. E. Cable, R. Huber, and J. G. Fujimoto, "Comparison of three-dimensional optical coherence tomography and high resolution photography for art conservation studies," Opt. Express **15**(24), 15972 (2007).

23. L. Carlyle and M. Witlox, "Historically accurate reconstructions of artists' oil painting materials," Tate Pap. **7** (2007).

24. B. Walter, S. R. Marschner, H. Li, and K. E. Torrance, "Microfacet models for refraction through rough surfaces," in *Proceedings of the 18th Eurographics conference on Rendering Techniques*, (Eurographics Association, 2007), pp. 195–206.

25. K. E. Torrance and E. M. Sparrow, "Theory for off-specular reflection from roughened surfaces," J. Opt. Soc. Am. **57**(9), 1105 (1967).

26. R. L. Cook and K. E. Torrance, "A reflectance model for computer graphics," ACM Trans. Graph. **1**(1), 7–24 (1982).

27. G. J. Ward, "Measuring and modeling anisotropic reflection," SIGGRAPH Comput. Graph. **26**(2), 265–272 (1992).

28. R. S. Berns and E. R. de la Rie, "The effect of the refractive index of a varnish on the appearance of oil paintings," Stud. Conserv. **48**(4), 251–262 (2003).

29. T. Akenine-Moller, E. Haines, and N. Hoffman, *Real-time rendering* (AK Peters/CRC, 2018).

30. J.-L. Delsaute, *The Camera Obscura and Painting in the Sixteenth and Seventeenth Centuries* (Yale University, 1998).

31. W. S. Elkhuizen, T. W. J. Callewaert, E. Leonhardt, A. Vandivere, Y. Song, S. C. Pont, J. M. P. Geraedts, and J. Dik, "Comparison of three 3D scanning techniques for paintings, as applied to Vermeer's 'Girl with a Pearl Earring'," Heritage Sci. **7**(1), 89 (2019).

32. J. Wadum, *Vermeer Illuminated: Conservation, Restoration and Research* (V+K Publishing/Inmerc, 1993).

33. J. C. Flores, "Mean-field crack networks on desiccated films and their applications: Girl with a Pearl Earring," Soft Matter **13**(7), 1352–1356 (2017).

34. A. Vandivere, ""Cloeck en veerdigh": energetic and skillful painting techniques of the sixteenth-century leiden school," JHNA **1**, 1 (2012).

35. M. Alfeld, J. V. Pedroso, M. van Eikema Hommes, G. V. der Snickt, G. Tauber, J. Blaas, M. Haschke, K. Erler, J. Dik, and K. Janssens, "A mobile instrument for in situ scanning macro-XRF investigation of historical paintings," J. Anal. At. Spectrom. **28**(5), 760 (2013).

36. W. D. Nolf, J. Dik, G. V. der Snickt, A. Wallert, and K. Janssens, "High energy X-ray powder diffraction for the imaging of (hidden) paintings," J. Anal. At. Spectrom. **26**(5), 910 (2011).